Nano Energy 32 (2017) 520–525

Contents lists available at ScienceDirect

Nano Energy

journal homepage: www.elsevier.com/locate/nanoen

Full paper

Enhanced thermoelectric properties in Bi/Te core/shell heterostructure nanowires through strain and interface engineering

Jeongmin Kim[a], Gwansik Kim[a], Je-Hyeong Bahk[b], Jin-Seo Noh[c], Wooyoung Lee[a,*]

[a] Department of Materials Science and Engineering, Yonsei University, 50 Yonsei-ro, Seodaemoon-gu, Seoul 03722, Republic of Korea
[b] Department of Mechanical and Materials Engineering, University of Cincinnati, OH 45221, USA
[c] Department of Nano-Physics, Gachon University, 1342 Seongnamdaero, Sujeong-gu, Seongnam-si, Gyeonggi-do 461-701, Republic of Korea

ARTICLE INFO

Keywords:
Core-shell nanowire
Strain engineering
Seebeck coefficient
Electrical conductivity
Thermal conductivity
Figure-of-merit (*ZT*)

ABSTRACT

Strain-engineered Bi/Te core/shell (C/S) nanowires (NWs) with various diameters were prepared by combining the on-film formation of NWs method with post-sputtering. Multiple devices were fabricated based on individual C/S NWs. The diameter-dependent electrical conductivity (σ), Seebeck coefficient (S), and thermal conductivity (κ) of the Bi/Te C/S NWs were systematically investigated. S and σ were found to increase with increasing NW diameter until they maximized at diameters exceeding 400 nm. Together with the reduction in κ, this generated a maximum thermoelectric figure of merit of 0.5 for a relatively large-diameter Bi/Te C/S NW (d=456 nm) at room temperature. These results suggest that the C/S NW structure could be used to modify the thermoelectric performance of materials, as the figure of merit was significantly greater than previously reported values for pure Bi NWs (0.07) and bulk Bi (0.05). Furthermore, the enhanced performance of very large Bi/Te C/S NWs demonstrated the possibility of designing heterostructures that can be used in thermoelectric device and module applications.

1. Introduction

In efforts to improve the performance of thermoelectric materials, nanostructures have been extensively investigated because they show unique properties, such as quantum confinement and phonon boundary scattering, at the nanoscale [1–4]. Despite promising theoretical expectations for nanostructured materials [5–8], however, only a few experimental results of the full thermoelectric performance of nanomaterials have been reported. This performance is represented by the dimensionless figure of merit $ZT=S^2\sigma T/\kappa$, where S, σ, T, and κ are the Seebeck coefficient, electrical conductivity, absolute temperature, and thermal conductivity, respectively [9,10]. This scarcity may stem from the lack of principles and methodologies required to synergistically control the individual thermoelectric parameters of nanostructures. Although a significant reduction in κ has been achieved in various nanostructure-based systems, the expected enhancement of S caused by the quantum confinement effect in nanostructures has not been substantially demonstrated [10–12]. Furthermore, the best thermoelectric performance for specific materials is generally predicted for the smallest possible nanostructures, which limit the practical applications of nanostructure-based thermoelectrics. In this regard, a recent study of the thermoelectric properties of Bi/Te core/shell (C/S) nanowires (NWs) with rough interfaces has provided an important method for controlling the thermoelectric performance of NW systems with fewer restrictions on the NW size [13]. In this study, because of the rough-interface effect, κ for the Bi/Te C/S NWs was found to be more than four times smaller than that for pure Bi NWs, even at large diameters ($d > 300$ nm). This range of diameters is promising because thermoelectric devices can be fabricated more easily using thick NWs. To estimate the full thermoelectric performance of the C/S NW system, however, the dependence of the various thermoelectric properties, including σ and S, on the NW diameter must be determined. As such, in this work, we thoroughly investigated the diameter dependence of σ, S, and κ for Bi/Te C/S NWs, thereby obtaining ZT trends. To the best of our knowledge, this is the first report of the full diameter-dependent performance of thermoelectric C/S NWs and the first determination of optimum performance for large-diameter NWs.

2. Experimental Section

2.1. Materials

Bi/Te C/S NWs were prepared using a combination of the on-film formation of NWs (OFFON) method and post-sputtering (Fig. 1a)

* Corresponding author.
E-mail address: wooyoung@yonsei.ac.kr (W. Lee).

http://dx.doi.org/10.1016/j.nanoen.2017.01.017
Received 21 October 2016; Received in revised form 17 December 2016; Accepted 8 January 2017
Available online 09 January 2017
2211-2855/ © 2017 Published by Elsevier Ltd.

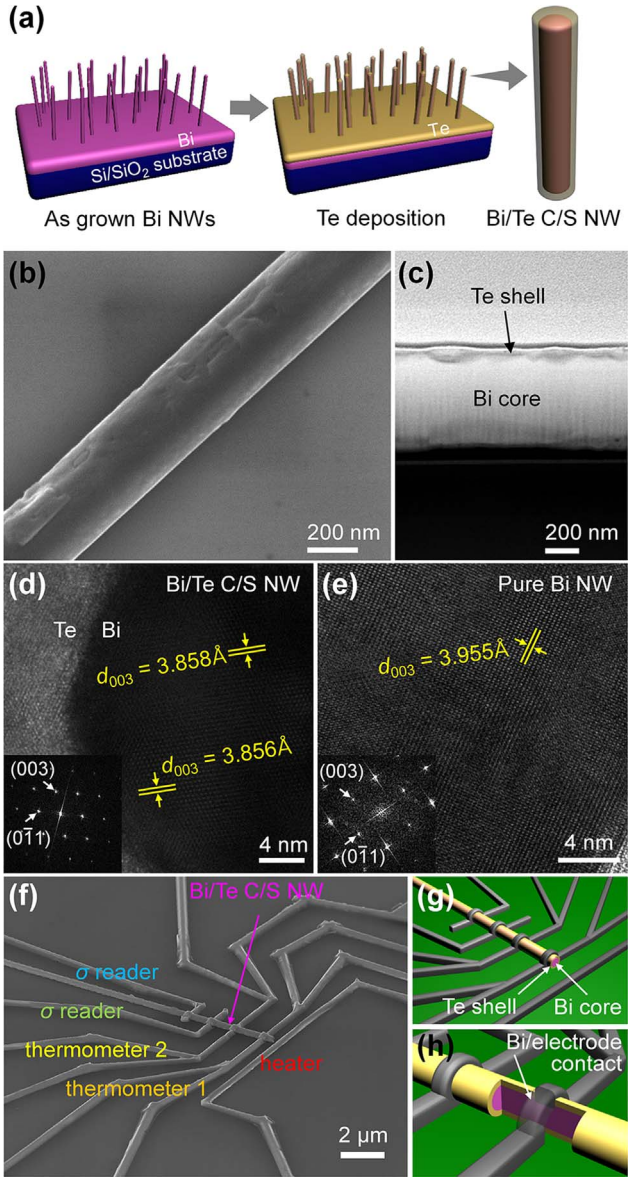

Fig. 1. Bi/Te C/S NW grown by the OFFON method and a thermoelectric device: (a) Representation of the growth mechanism and C/S structure of Bi/Te NW grown on Si/SiO_2 substrate. (b) SEM image of as-grown Bi/Te C/S NW. (c) LMTEM image of Bi/Te C/S NW sliced along the NW direction. (d) Cross-sectional HRTEM image of Bi/Te C/S NW sliced normal to the NW direction. Inset: SAED pattern confirming single-crystalline NW growing in the [100] direction. (e) HRTEM image of pure Bi NW. Inset: SAED pattern. (f) SEM image of 456-nm-diameter device based on an individual Bi/Te C/S NW used for σ and S measurements. Schematics of (g) the NW device and (h) contact region.

[13,14]. The Bi core NWs were grown from Bi films deposited on thermally oxidized Si (100) substrates during thermal annealing at 250 °C for 5 h. The Te shell was subsequently sputter-deposited at a radio frequency (RF) power of 30 V under an ultra-high vacuum of 10^{-7} Torr. The diameters of the Bi/Te C/S NWs were varied from 61 to 850 nm for a fixed Te shell thickness of 30 nm. The uniform diameter of the NWs was confirmed by scanning electron microscope (SEM) imaging, even though slight surface roughness caused by the formation of a rough interface was observed (Fig. 1b). The uniformity of the Te shell thickness on the NWs was confirmed for diameters > 100 nm. However, the Te layer was typically less than 30 nm thick on NWs of smaller diameters. A transmission electron microscope (TEM) was used to analyze the crystalline structure of the Bi/Te C/S NWs. The rough interface between the Bi core and Te shell was confirmed by low-magnification TEM (LMTEM) imaging, as shown in Fig. 1c (Fig. S1, Supplementary materials). Selected-area electron diffraction (SAED) and high-resolution TEM (HRTEM) imaging show that the Bi/Te C/S NW grows as a single crystal in the [100] direction with 3.86 Å-spaced lattice fringes (Fig. 1d). This spacing matches the interplanar spacing of the (003) planes of Bi. The lattice parameter of 11.58 Å is found in the [001] direction, which is ~2.5% smaller than that of the pure Bi NW (c=11.87 Å), as shown in Fig. 1e (Fig. S2, Supplementary materials).

2.2. Methods

The thermoelectric devices fabricated using the Bi/Te C/S NWs consist of a microheater, thermometer 1 (TM1), thermometer 2 (TM2), and σ readers (Fig. 1f). The Bi/Te C/S NWs were dispersed onto a thermally oxidized Si (100) substrate with large contact pads patterned by photolithography and a lift-off process. A combination of E-beam lithography and a lift-off process was employed to fabricate micrometer-scale inner electrodes of Cr (5 nm)/Au (100–300 nm). A plasma etching process was used to remove the oxide layer from the outer surface of the NWs and the Te shells immediately before the electrode materials were deposited. This oxide removal enabled the formation of an effective ohmic contact between the NWs and the electrode materials (Fig. 1g and h). Etching to remove the oxide layer and the electrode deposition were performed in-situ without breaking the vacuum in order to prevent further oxide formation [15,16].

S for the NW was measured by producing a temperature gradient on the SiO_2/Si substrate using the microheater [17,18]. A bias voltage was applied to the heater line in order to generate joule heat, thereby increasing the temperature of the heater. The heat generated was designed to propagate through a 0.5-μm-thick SiO_2 layer, creating a temperature gradient across the Bi NW placed in thermal contact with the SiO_2 layer. The temperature difference (ΔT) was determined from the temperatures of the NW-electrode junctions measured at TM1 and TM2 using the four-probe method. In this work, the distance from the heater to TM1 and the spacing between TM1 and TM2 were 1 and 2 μm, respectively. The Seebeck voltages (ΔV) across the Bi/Te C/S NW were measured with a nanovoltmeter. From the measured ΔT and ΔV, S for the Bi/Te C/S NW was calculated from the equation $S=\Delta V/\Delta T$, since it was confirmed that $\Delta V \propto I_h^2 \propto \Delta T$ [10]. σ of the NW was measured using a conventional four-terminal geometry, which excluded contributions from the contact resistance. Measurements for σ and S were both performed in direct-current (DC) mode at room temperature. A detailed description of thermoelectric measurements based on single NWs is available in Ref. 10.

3. Results and discussion

3.1. Strain electronic band engineering

Fig. 2 shows the highly anisotropic electronic band structure of rhombohedral Bi in momentum space. The first Brillouin zone of Bi is compressed along the trigonal direction owing to the asymmetrical crystal structure being stretched along the c-axis in real space (Fig. 2a) [19]. Because of this anisotropy, Bi has different band energies at the L- and T-points in the Brillouin zone, resulting in semimetallic characteristics with small band overlap, as shown in Fig. 2b [20]. Therefore, the band structure of Bi can be effectively controlled by deformation of its crystal structure. Particularly, compressive strain along the c-axis leads to an elongation of the Brillouin zone along the trigonal direction, resulting in a decrease of band overlap energy (Fig. 2c) [21,22]. In this concept, a significantly reduced diameter for the quantum size effect (QSE) is not needed for band engineering. Moreover, because modification of the band structure is dominant at the T-point, it is not necessary to consider the strong coupling effect at the L-point, which increases the electron effective mass [16]. Therefore, it is possible to

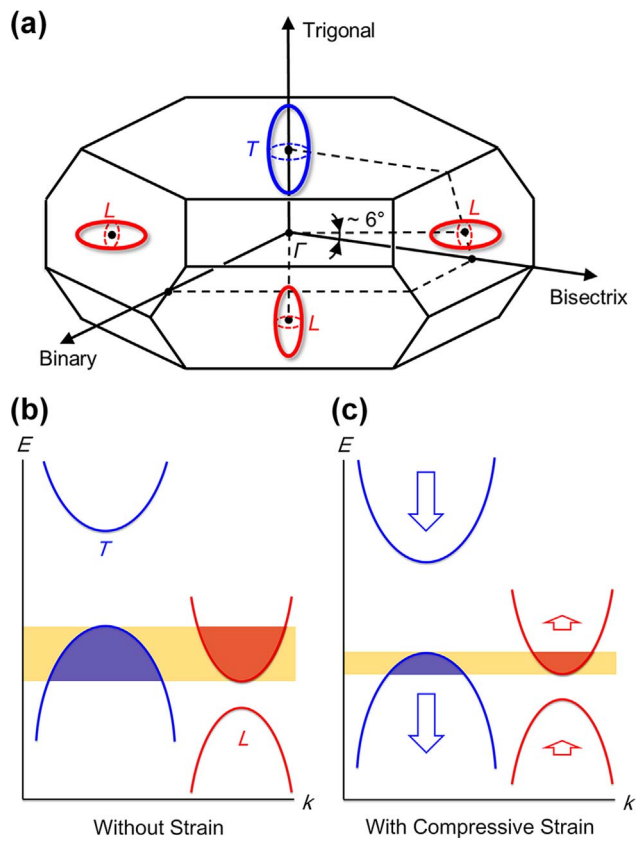

Fig. 2. Electronic band structure of Bi and strain effect: (a) Highly anisotropic Brillouin zone of rhombohedral Bi with L-point electron pockets and T-point hole pockets. (b) Band overlap energy between the L-point conduction band and T-point valence band in semimetallic Bi. (c) Reduction of band overlap energy caused by compressive strain along the *c*-axis of Bi.

demonstrate effectively the enhancement of S due to a decrease in band overlap energy without the negative effects reported in QSE band engineering [8,10].

3.2. Diameter-dependent electrical conductivity

Fig. 3a shows the diameter-dependent σ for Bi/Te C/S NWs measured at room temperature. In general, σ decreases with decreasing diameter because of the reduced mobility of the charge carriers. A similar trend has been observed in pure Bi NWs [10,19,23]. The main difference in the diameter dependence of σ between pure Bi and Bi/Te C/S NWs is the critical diameter, below which the resistivity decreases from the saturation level. The Bi/Te C/S and pure Bi NWs have critical diameters of ~400 nm and ~100 nm, respectively [10,23]. This difference stems from the differing relative contributions of the Bi core and Te shell to the total conductance. The conductive systems were arranged in parallel combination and the total conductivity (σ_{total}) was calculated for variations in the partial conductance values of the Bi core and Te shell, defined as $G_{core,\ Bi}=\sigma_{core,\ Bi}\ (A_{core,\ Bi}/L)$ and $G_{shell,\ Te}=\sigma_{shell,\ Te}\ (A_{shell,\ Te}/L)$, respectively. Here, G, L, and A are the respective conductance, length of the channel, and cross-sectional area of the channel. The total conductance of a Bi/Te C/S NW is given by $G_{total}=\sigma_{total}\ (A_{total}/L)=G_{core,\ Bi}+G_{shell,\ Te}$. Hence, the σ_{total} can be expressed as

$$\sigma_{total} = \frac{\sigma_{core,Bi}A_{core,Bi} + \sigma_{shell,Te}A_{shell,Te}}{A_{core,Bi} + A_{shell,Te}}. \quad (1)$$

Since the σ of Te (2–100 Ω^{-1} cm^{-1}) is significantly smaller than that of the Bi NW (5000 Ω^{-1} cm^{-1}), σ_{total} should decrease with an increase in the fraction of Te [23–25]. This decrease occurs gradually with

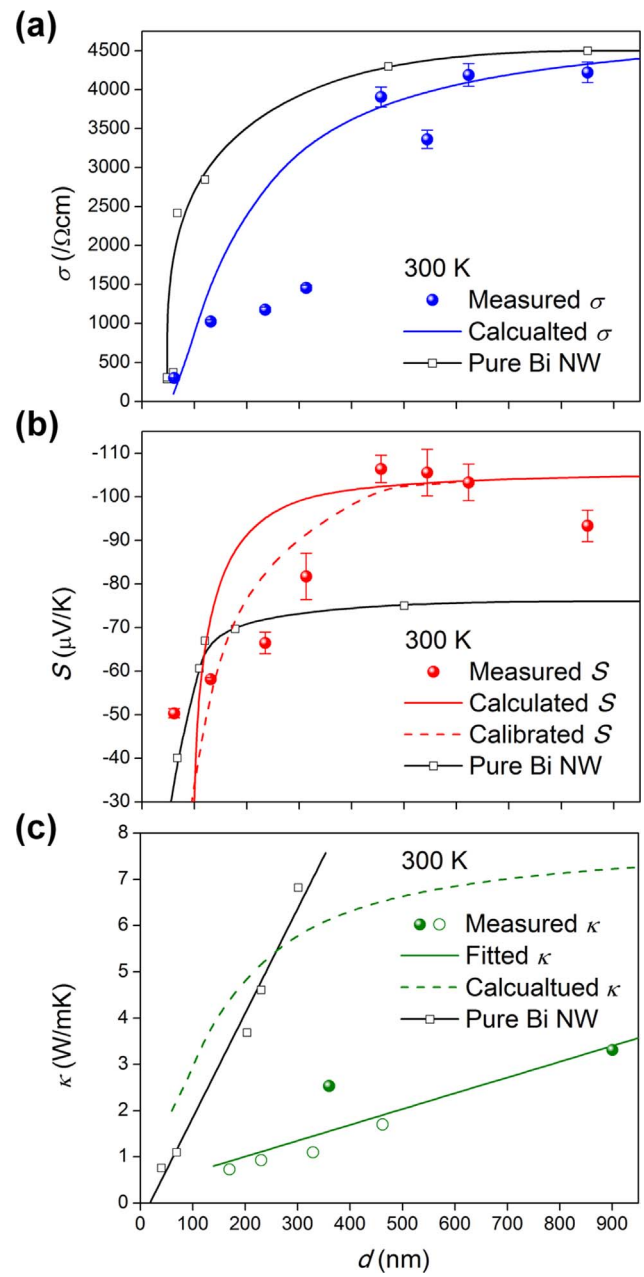

Fig. 3. Diameter-dependent thermoelectric transport properties of Bi/Te C/S NW: (a) σ of Bi/Te C/S NWs for diameters of 61, 131, 235, 313, 456, 544, 623, and 850 nm. Some points are plotted without error bars, because the error is smaller than the data markers for these cases. Blue line: calculated σ for a parallel combination of conductive systems. (b) S for Bi/Te C/S NWs. Solid and dashed red lines represent calculated and calibrated S, respectively, based on a parallel combination of the thermoelectric system. (c) κ of Bi/Te C/S NWs. Solid and open green symbols denote κ measured by suspended devices from this work and our previous study (Ref. 11), respectively. The solid green line shows the extrapolated κ obtained from the measured data. The dashed green line represents the calculated κ according to a parallel combination of conductive systems. The thermoelectric properties of pure Bi NWs are reproduced from our previous study (Ref. 10) for comparison. The black line is present for visual guidance.

decreases in the diameter of the Bi/Te C/S NWs, since the Te shell thickness is fixed at 30 nm in this work. The diameter dependence of σ, calculated using Eq. (1) (Fig. 3a) is similar to that measured from Bi/Te C/S NWs (Fig. S3, Supplementary materials). The deviation between these trends in the range of 200–400 nm results from the decreased σ of the Bi core; this decrease also occurs in pure Bi NWs, stemming from the QSE-induced reduction in the carrier mobility and concentration

[10]. For pure Bi NWs, the decrease in diameter creates a strong coupling effect in the L-point sub-bands. This coupling, in turn, increases the carrier effective mass and decreases the σ for diameters lower than 100 nm [10,16]. Moreover, the reduced electronic band overlap between the L-point conduction and T-point valence bands decreases the carrier concentration, which also reduces the σ [10,16]. In Bi/Te C/S NWs, however, this effect is more dominant at large diameters than it was for pure Bi NWs. This is attributed to the change in electronic band structure because of strain in the Bi core. The compressive strain along the trigonal direction of Bi increases the L-point band gap and decreases the band overlap energy [21,22]. Consequently, the diameter-dependent reduction in σ occurs at a larger diameter (400 nm) of the Bi core than that for pure Bi (100 nm) [10].

3.3. Diameter-dependent Seebeck coefficient

Fig. 3b shows the diameter dependence of S for the Bi/Te C/S NWs. The negative S value indicates that electrons are the major carriers, as in pure Bi NWs [10]. In addition, because of the strain-induced modification of the electronic band, S for large-diameter (d=~500 nm) Bi/Te C/S NWs is 150% of that of the pure Bi NWs [10]. However, compared to that of the pure Bi NWs, the absolute value of S is decreased more rapidly with decreases in the diameter of the Bi/Te C/S NWs. This diameter dependence contradicts certain predictions of NW thermoelectrics, which have proposed S enhancements with reduced NW size [7,8]. The discrepancy between our results and those of both previous studies and theoretical predictions can be attributed to three factors. First, the core material, Bi, has equal and very low concentrations of electrons and holes (n=p=2×10^{18} cm^{-3}) [14,26,27]. S for a material containing both electrons and holes can be expressed as an average of the σ-weighted partial S values of the individual bands [5]. For indirect conduction and valence bands, as in Bi, the total coefficient is given by $S_{total}=(\sigma_e S_e+\sigma_h S_h)/(\sigma_e+\sigma_h)$, where the subscripts e and h refer to electrons and holes, respectively [5]. Therefore, the contribution from the holes to the total S value approximately cancels that from the electrons, generating a very low S. The total S is highly sensitive to the concentrations and effective masses, or weighting factors, of both carrier types [5,23,28]. Second, the change in the electronic band structure by compressive strain in the Bi core is increased over a particular range of diameters. This range depends on the negative effects of diameter decrease, as observed in pure Bi NWs [10]. As previously mentioned in 3.1, reducing the diameter of Bi increases the band gap of the L-point sub-band and decreases the band overlap energy between the L- and T-points. This, in turn, increases and decreases the effective mass and concentration, respectively, of carriers. These changes in the effective mass and concentration cause reductions in the weighting factors (σ_e) of S_e, thereby decreasing the total S of the pure Bi NWs [10,29]. In the Bi/Te C/S NWs, the increased band gap of the L-point and decreased band overlap energy, caused by the compressive strain, accelerate the negative effects of diameter reduction. Therefore, the decrease in S_{total} of the Bi/Te C/S NWs begins at a much larger diameter (400 nm) than that for the pure Bi NWs (100 nm) [10]. In addition, σ and S of both pure Bi and Bi/Te C/S NWs change rapidly in the same diameter range. This indicates that the change in the thermoelectric properties can be attributed to the variation of intrinsic properties caused by diameter reduction. Third, the parallel combination of the two thermoelectric systems should be considered. The Bi/Te C/S NWs contain both Bi and Te, whose S values differ significantly in both sign and magnitude; S_{Bi}≈−70 μV K^{-1} and S_{Te}≈500 μV K^{-1}. When the Bi core and Te shell are combined in parallel, the total S is weighted by the conductance, rather than the σ, of each component and is defined as follows:[30].

$$S_{total} = \frac{G_{core,Bi}S_{core,Bi} + G_{shell,Te}S_{shell,Te}}{G_{core,Bi} + G_{shell,Te}}. \quad (2)$$

The area fraction of the Te shell increases as the diameter decreases, thereby increasing the contribution of the shell to S for the Bi/Te C/S NWs. Furthermore, Eq. (2) indicates that, with decreasing diameter, the positive S of the shell will gradually cancel out the negative S of the core, as shown in Fig. 3b. In this calculation, S for the large-diameter Bi core is assumed to be 150% of that of pure Bi, as demonstrated in previous theoretical and experimental studies [10]. The total S can still be calculated, despite the assumption that $S_{shell,Te}$=S_{Te}, because the weighting factor of the shell is significantly smaller than that of the core. The large deviation at the smallest diameter can be ignored, because the diameter of the core becomes negligible with the fixed shell thickness used in the calculation. However, the deviation between the calculated and measured S arises because the calculation is performed for a simple parallel combination with the calculated conductance values. This deviation can be reduced by using the conductance of the Bi core, which is subtracted from the measured σ. While this method does reduce the aforementioned difference, a slight deviation persists for diameters of 200–400 nm; this slight deviation is attributed to the previously described negative effect of the QSE-induced reduction in diameter [10,16]. The results are consistent with that obtained for σ (Fig. S4, Supplementary materials).

3.4. Diameter-dependent thermal conductivity

Fig. 3c shows the diameter-dependent κ of the Bi/Te C/S NWs at room temperature, as measured using a suspended device as explained in detail elsewhere [13,31]. To determine the diameter-dependency accurately, additional data points obtained from Bi/Te C/S NWs grown by an identical procedure are reproduced from our previous study [13]. κ is decreased with decreasing diameter, as it is for pure Bi NWs and typical nanostructured materials [10,31]. Moreover, κ of the Bi/Te C/S NWs is more than four times smaller than that of even large-diameter (d > 320 nm) pure Bi NWs; this low κ is caused by phonon scattering at the rough core-shell interface [13]. To distinguish the rough interface effect, the parallel combination of conductive systems is employed as in [32]:

$$\kappa_{total} = \frac{\kappa_{core,Bi}A_{core,Bi} + \kappa_{shell,Te}A_{shell,Te}}{A_{core,Bi} + A_{shell,Te}}, \quad (3)$$

We assume that $\kappa_{core,Bi}$ and $\kappa_{shell,Te}$ are 8 and 2 W m^{-1} K^{-1}, respectively. Because this model ignores the rough interface effect, the discrepancies between the measured and calculated data indicate the heterogeneous Bi/Te interface effect [32]. We used extrapolations to estimate κ at specific diameters, instead of directly measuring κ, although σ and S measurements were made. In these cases, κ is assumed to exhibit a linear dependency on the NW diameter [13]. The fact that the decrease in thermal conductivity is larger than that in electrical conductivity indicates a reduction in the lattice thermal conductivity (κ_L). The κ_L value can be extracted from the total κ by subtracting the electronic thermal conductivity (κ_e), which is determined by the Wiedemann–Franz law, κ_e=$L\sigma T$, where L is the Lorenz number. Usually, the values of L vary from 2.44×10^{-8} W Ω K^{-2} for non-degenerated semiconductors to 2.44×10^{-8} W Ω K^{-2} for metals and strongly degenerated semiconductors [33,34]. Because our C/S NWs consist of a semimetal/semiconductor heterostructure, L is expected to lie between these two limiting values. We calculated L using the reduced Fermi energy obtained from the measured S value at different diameters (Supplementary materials). The calculated L decreased slightly as decreasing diameter above ~300 nm, which is in good agreement with previous studies on thermoelectric NWs, as shown in Fig. 4a [35–38]. Below diameters of ~300 nm, however, L increased sharply because of the rapid decrease in σ caused by the fixed Te shell thickness and increased contact resistance. Fig. 4b shows the κ_e and κ_L values as a function of diameter. Above ~300 nm, both κ_e and κ_L decrease with decreasing diameter due to the size effect and interface

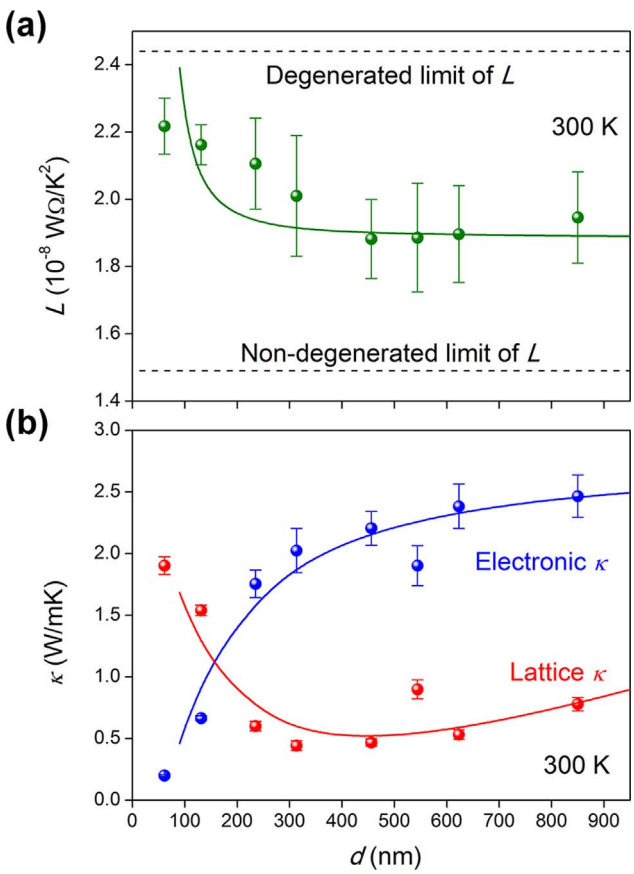

Fig. 4. Electronic and lattice components of thermal conductivity: (a) Calculated L and (b) electronic κ and lattice κ as a function of diameter. The colored symbols and lines indicate the obtained results based on the measured and calculated data, respectively, in Fig. 3.

scattering in the NWs. The sharp increase in κ_L below ~300 nm is attributed to an overestimated L value.

3.5. Theoretical simulation of strain and doping effects

The other factors caused by the Te shell also change S. The interaction between the Bi core and Te shell is neglected in the simple parallel combination of thermoelectric systems. However, the role of Te as an electrical dopant, increasing the electron concentration (n) in the Bi core, must be considered. Furthermore, the smaller c-axis lattice parameter of Te compared to that of Bi (5.9290 Å vs. 11.862 Å) induces a compressive strain in the core, as previously mentioned [39,40]. This, in turn, causes the contraction of the c-axis and hence variations in the band overlap and carrier concentration of the core [21,22]. This strain effect is observed both at the interface and within the core. Fig. 5 shows the calculated σ and S of the Bi core as functions of n, based on the Boltzmann transport equation. Reduction in the band overlap caused by the strain effect shifted the S and σ curves. In an n range similar to that of Bi, S increased while σ decreased slightly in accordance with the experimental results (Fig. 3a and b). It was found that n, estimated from the measured thermoelectric properties, was constant at ~2×10^{18} cm^{-3}, despite the decrease in band overlap energy. This may be because the doping effect due to the Te shell compensates for the decrease of n caused by the decrease in band overlap energy.

3.6. Diameter-dependent power factor and figure of merit

As previously mentioned in Section 1, the comprehensive thermoelectric performance of a system is represented by ZT, which depends on the power factor $S^2\sigma$ and κ. A high ZT combines a large power factor

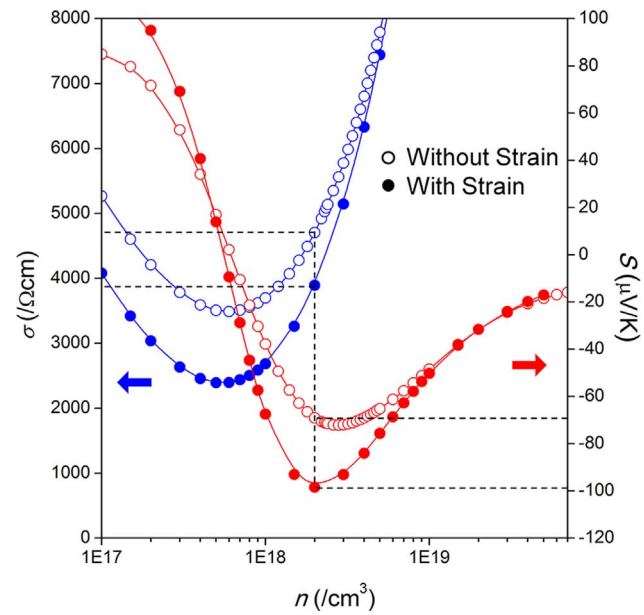

Fig. 5. Effect of band overlap reduction on σ and S for different n values. Blue and red represent σ and S, respectively. The solid and open symbols show the calculated results with (−2.5%) and without strain, respectively. The horizontal dashed lines indicate the values obtained experimentally and the vertical dashed line indicates the value of n estimated by the theoretical calculation based on measured thermoelectric properties.

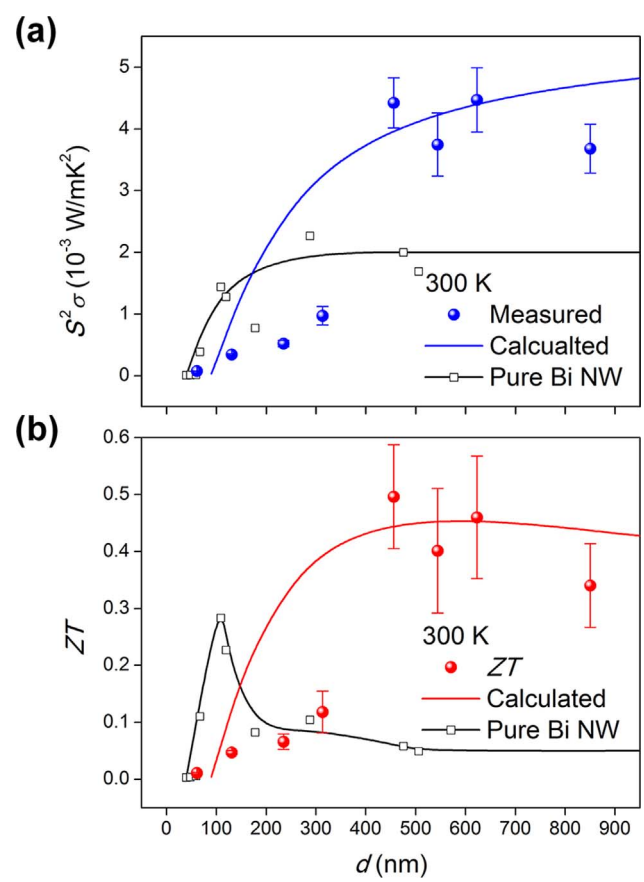

Fig. 6. Diameter-dependent thermoelectric power factor and ZT for Bi/Te C/S NWs: (a) Power factor (blue symbols) and (b) ZT (red symbols) obtained from the measured thermoelectric properties. Colored lines show the calculated diameter-dependent power factor (blue) and ZT (red). The data for pure Bi NWs were reproduced from our previous study (Ref. [10]) for comparison. The black lines (solid or dashed) are present for visual guidance.

with a small κ value. $S^2\sigma$ for Bi/Te C/S NWs with various diameters is obtained from the measured values and shown in Fig. 6a. Here, the extrapolated κ values are determined over a broad range of diameters, and are especially reliable at large diameters (Fig. 3c). $S^2\sigma$ is increased with increases in diameter up to 400 nm, reaching a maximum value of 4.42×10^{-3} W m^{-1} K^{-2} at a diameter of 456 nm, thereby verifying the diameter dependence of σ and S. As Fig. 3a and b show, σ and S both increase with increasing diameter until reaching saturation at ~400 nm, with maximum values at 456 nm of σ_{max}=3910 Ω^{-1} cm^{-1} and $|S_{max}|$=106.4 μV K^{-1}. The diameter-dependent ZT of Bi/Te C/S NWs is obtained from $S^2\sigma$ and κ, as shown in Fig. 6b. As with $S^2\sigma$, ZT is increased with increases in diameter and reaches a maximum value at a diameter of 456 nm. ZT varies in the same manner as S because, for diameters of 61–456 nm, $S^2\sigma$ changes more dramatically than κ. After reaching a maximum value, ZT decreases with further increases in the diameter because of the additional increases in κ. Surprisingly, a very high ZT of 0.5 is achieved in a thick 456-nm-diameter Bi/Te C/S NW. This ZT value is significantly greater than the previously reported values of pure Bi NWs (0.07) and bulk Bi (0.05) and is the highest value ever reported for Bi-based hetero-NWs [10]. Moreover, the NW diameter (456 nm) at which the maximum ZT occurs is significantly larger than those at which the best ZTs were experimentally obtained (in rough Si NWs) or theoretically predicted (for pure Bi NWs) in previous studies. This indicates that, in some NWs, $S^2\sigma$ prevails over κ in determining ZT; Bi/Te C/S NWs exemplify such NW systems.

Finally, the transport properties of the shell should be considered in order to enhance the thermoelectric performance using heterostructure C/S NWs. As described above, the increase in ZT was demonstrated in Bi/Te C/S NWs using strain and interface engineering based on the Te shell. According to Eqs. (1)–(3), transport phenomena in the shell affect the total properties of the overall C/S structure. Therefore, in order to effectively use the enhanced S of the core, the contribution of the core to the total properties should be increased. In the case of strain engineering, it is preferable that the partial conductance of the shell be lower than that of the core according to Eq. (2). Moreover, to reduce the total κ of the C/S structure, low-κ materials should be used for the shell. Therefore, it can be predicted that Bi/insulator C/S NWs will be more effective in terms of thermoelectric performance than Bi/semiconductor and Bi/metal C/S NWs, even though it is necessary to optimize the shell thickness according to the materials used.

4. Conclusion

We systematically investigated the diameter dependence of the thermoelectric figure of merit ZT in Bi/Te C/S NWs by varying the NW diameter from 61 to 850 nm. The power factor, as calculated from the measured values, was increased with increasing diameter and was maximized at a diameter of ~400 nm; in contrast, κ, as extrapolated from the obtained diameter dependence, increased more gradually. These diameter-dependent variables generated a very high ZT of 0.5 for a thick 456-nm-diameter Bi/Te C/S NW. This is far higher than those measured for pure Bi NWs (0.07) and bulk Bi (0.05). Furthermore, the enhanced performance of very large Bi/Te C/S NWs suggests the possibility of designing heterostructures that can be used in thermoelectric device and module applications.

Acknowledgment

This work was supported by the National Research Foundation of Korea (NRF) Grant funded by the Korea government (MSIP) (2014R1A2A1A10053869) and the Priority Research Centers Program (2009-0093823).

Appendix A. Supporting information

Supplementary data associated with this article can be found in the online version at doi:10.1016/j.nanoen.2017.01.017.

References

[1] K. Biswas, J. He, Q. Zhang, G. Wang, C. Uher, V.P. Dravid, M.G. Kanatzidis, Nat. Chem. 3 (2011) 160–166.
[2] R. Venkatasubramanian, E. Siivola, T. Colpitts, B. O'Quinn, Nature 413 (2001) 597–602.
[3] G. Zhang, Q. Yu, W. Wang, X. Li, Adv. Mater. 22 (2010) 1959–1962.
[4] G. Zhang, W. Wang, X. Li, Adv. Mater. 20 (2008) 3654–3656.
[5] L.D. Hicks, M.S. Dresselhaus, Phys. Rev. B: Condens. Matter Mater. Phys. 47 (1993) 12727–12731.
[6] L.D. Hicks, M.S. Dresselhaus, Phys. Rev. B: Condens. Matter Mater. Phys. 47 (1993) 16631–16634.
[7] M.S. Dresselhaus, G. Dresselhaus, X. Sun, Z. Zhang, S.B. Cronin, T. Koga, Phys. Solid State 41 (1999) 679–682.
[8] Y.M. Lin, X.Z. Sun, M.S. Dresselhaus, Phys. Rev. B: Condens. Matter Mater. Phys. 62 (2000) 4610–4623.
[9] A. Majumdar, Science 303 (2004) 777–778.
[10] J. Kim, S. Lee, Y.M. Brovman, P. Kim, W. Lee, Nanoscale 7 (2015) 5053–5059.
[11] A.I. Hochbaum, R. Chen, R.D. Delgado, W. Liang, E.C. Garnett, M. Najarian, A. Majumdar, P. Yang, Nature 451 (2008) 163–167.
[12] A. Boukai, K. Xu, J.R. Heath, Adv. Mater. 18 (2006) 864–869.
[13] J. Kang, J.W. Roh, W. Shim, J. Ham, J.-S. Noh, W. Lee, Adv. Mater. 23 (2011) 3414–3419.
[14] W. Shim, J. Ham, K.I. Lee, W.Y. Jeung, M. Johnson, W. Lee, Nano Lett. 9 (2009) 18–22.
[15] J. Kim, S. Lee, Y.M. Brovman, M. Kim, P. Kim, W. Lee, Appl. Phys. Lett. 104 (2014) 043105.
[16] J. Kim, D. Kim, T. Chang, W. Lee, Appl. Phys. Lett. 105 (2014) 123107.
[17] J.P. Small, K.M. Perez, P. Kim, Phys. Rev. Lett. 91 (2003) 256801.
[18] Y.M. Zuev, J.S. Lee, C. Galloy, H. Park, P. Kim, Nano Lett. 10 (2010) 3037–3040.
[19] J. Kim, W. Shim, W. Lee, J. Mater. Chem. C 3 (2015) 11999–12013.
[20] P. Hofmann, Prog. Surf. Sci. 81 (2006) 191–245.
[21] J.R. Vaišnys, R.S. Kirk, J. Appl. Phys. 38 (1967) 4335–4337.
[22] M. Kasami, T. Ogino, T. Mishina, S. Yamamoto, J. Nakahara, J. Lumin. 119–120 (2006) 428–432.
[23] J. Heremans, C.M. Thrush, Phys. Rev. B: Condens. Matter Mater. Phys. 59 (1999) 12579–12583.
[24] A. Nussbaum, Phys. Rev. 94 (1954) 337–342.
[25] V.E. Bottom, Science 115 (1952) 570–571.
[26] Z.B. Zhang, X.Z. Sun, M.S. Dresselhaus, J.Y. Ying, J. Heremans, Phys. Rev. B: Condens. Matter Mater. Phys. 61 (2000) 4850–4861.
[27] J. Heremans, C.M. Thrush, Y.M. Lin, S. Cronin, Z. Zhang, M.S. Dresselhaus, J.F. Mansfield, Phys. Rev. B: Condens. Matter Mater. Phys. 61 (2000) 2921–2930.
[28] J.P. Heremans, C.M. Thrush, D.T. Morelli, M.-C. Wu, Phys. Rev. Lett. 88 (2002) 216801.
[29] T.W. Cornelius, M.E.T.– Molares, Nanowires, InTech, Shanghai, 2010.
[30] T.E. Huber, A. Adeyeye, A. Nikolaeva, L. Konopko, R.C. Johnson, M.J. Graf, Phys. Rev. B: Condens. Matter Mater. Phys. 83 (2011) 235414.
[31] J.W. Roh, K. Hippalgaonkar, J.H. Ham, R.K. Chen, M.Z. Li, P. Ercius, A. Majumdar, W. Kim, W. Lee, ACS Nano 5 (2011) 3954–3960.
[32] T.-K. Hsiao, B.-W. Huang, H.-K. Chang, S.-C. Liou, M.-W. Chu, S.-C. Lee, C.-W. Chang, Phys. Rev. B: Condens. Matter Mater. Phys. 91 (2015) 035406.
[33] V.I. Fistul, Heavily Doped Semiconductors, Plenum Press, New York, 1969.
[34] T.M. Tritt, Thermal Conductivity, Kluwer Academic/Plenum Publisher, New York, 2004.
[35] F. Völklein, H. Reith, T.W. Cornelius, M. Rauber, R. Neumann, Nanotechnology 20 (2009) 325706.
[36] F. Völklein, H. Reith, M.C. Schmitt, M. Huth, M. Rauber, R. Neumann, J. Electron. Mater. 39 (2010) 1950–1956.
[37] E.Z. Xu, Z. Li, J.A. Martinez, N. Sinitsyn, H. Htoon, N. Li, B. Swartzentruber, J.A. Hollingsworth, J. Wang, S.X. Zhang, Nanoscale 7 (2015) 2869–2876.
[38] C.-H. Chien, P.-C. Lee, W.-H. Tsai, C.-H. Lin, C.-H. Lee, Y.-Y. Chen, Sci. Rep. 6 (2016) 23672.
[39] W.M. Haynes, CRC Handbook of Chemistry and Physics, CRC Press, 2012.
[40] C.S.B.D. Schiferl, J. Appl. Crystallogr. 2 (1969) 30–36.